Cellulose (2024) 31:515–534
https://doi.org/10.1007/s10570-023-05601-1

ORIGINAL RESEARCH

Cellulose-in-cellulose 3D-printed bioaerogels for bone tissue engineering

Ana Iglesias-Mejuto · Nanthilde Malandain · Tânia Ferreira-Gonçalves · Inés Ardao · Catarina Pinto Reis · Anna Laromaine · Anna Roig · Carlos A. García-González

Received: 3 July 2023 / Accepted: 6 November 2023 / Published online: 12 December 2023

Abstract Nanostructured scaffolds based on cellulose with advanced performances and personalized morphologies for bone tissue engineering are under technological development. 3D-printing and supercritical carbon dioxide ($scCO_2$) technologies are innovative processing strategies that, when combined, allow the precise fabrication of highly porous aerogel scaffolds. Novel sterile cellulose-in-cellulose aerogels decorated with superparamagnetic iron oxide nanoparticles (SPIONs) are synthesized in this work by an integrated technological platform based on 3D-printing and $scCO_2$. Methylcellulose (MC) and bacterial nanocellulose (BC) are two versatile cellulosic polysaccharides with remarkable physicochemical and biological performances, whereas SPIONs are commonly used to functionalize biomaterials aimed at tissue engineering. Aerogels with hierarchical porosity and high structural resolution were obtained according to nitrogen adsorption–desorption analysis, confocal, scanning and transmission microscopies (SEM and TEM). The magnetic properties of SPIONs-doped aerogels confirmed the correct functionalization of the nanostructures. Finally, NIH/3T3 fibroblast cell viability, hemocompatibility with human blood and safety tests (*in ovo* with HET-CAM and in vivo with *Artemia salina*) indicate the biocompatibility of the cellulose-in-cellulose aerogels.

A. Iglesias-Mejuto · C. A. García-González (✉)
AerogelsLab, I+D Farma Research Group (GI-1645), Department of Pharmacology, Pharmacy and Pharmaceutical Technology, Faculty of Pharmacy, iMATUS and Health Research Institute of Santiago de Compostela (IDIS), Universidade de Santiago de Compostela, 15782 Santiago de Compostela, Spain
e-mail: carlos.garcia@usc.es

N. Malandain · A. Laromaine · A. Roig
Institut de Ciència de Materials de Barcelona, ICMAB-CSIC, Campus UAB, 08193 Bellaterra, Spain

N. Malandain
Unitat de Biofísica i Bioenginyeria, Facultat de Medicina i Ciències de la Salut, Universitat de Barcelona, 08036 Barcelona, Spain

T. Ferreira-Gonçalves · C. P. Reis
Research Institute for Medicines (iMed.ULisboa), Faculty of Pharmacy, Universidade de Lisboa, Av. Professor Gama Pinto, 1649-003 Lisbon, Portugal

T. Ferreira-Gonçalves · C. P. Reis
Instituto de Biofísica e Engenharia Biomédica (IBEB), Faculdade de Ciências, Universidade de Lisboa, 1749-016 Campo Grande, Lisbon, Portugal

I. Ardao
BioFarma Research Group, Department of Pharmacology, Pharmacy and Pharmaceutical Technology, Innopharma Drug Screening and Pharmacogenomics Platform, Centro Singular de Investigación en Medicina Molecular y Enfermedades Crónicas (CiMUS), Universidade de Santiago de Compostela, 15782 Santiago de Compostela, Spain

Graphical abstract

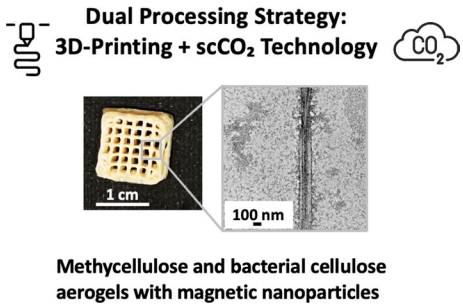

Keywords Aerogels · Supercritical carbon dioxide · 3D-printing · Nanocellulose · SPIONs

Introduction

Clinically treating large bone lesions resulting from tumor ablation, trauma, or bone fractures require autologous tissues, allografts, or bone graft substitutes for long-term regeneration (Feng et al. 2021). Due to the limited availability of biological grafts and the increment in the morbidity associated with tissue transplants, emerging technologies are proliferating to fabricate bone tissue substitutes (Qu et al. 2021). Biocompatible, highly porous, and hierarchical architectures capable of host blood-biomaterial interaction and harboring neo-tissue regeneration are critical factors when designing bone tissue substitutes (Zhao et al. 2016; Qu et al. 2021).

Natural biopolymers and their derivatives (e.g., methylcellulose (MC), hydroxypropyl cellulose, or hyaluronic acid) have often been used in bone tissue engineering because of their hydrophilicity, biocompatibility, and bioadhesiveness (Li and Chen 2015; Gerasimenko et al. 2020). The incorporation of these biopolymers into scaffolds can improve the osseointegration, inflammation, and bone healing if adequately designed from the composition and morphological points of view (Zhao et al. 2016; Gerasimenko et al. 2020). Bioaerogels, i.e., aerogels obtained from natural polymers, are mesoporous and nanostructured materials with outstanding physicochemical performances and relevant properties for biomedical applications like biocompatibility or biodegradability (Maleki et al. 2016; Budtova 2019; Budtova et al. 2020; Bernardes et al. 2021). The medical field quests to translate those requirements to 3D scaffolds with precise features and replication of functional human native systems (Wang et al. 2022). Specifically, 3D printing technologies are being explored for bone lesion management to manufacture reproducible and scalable scaffolds with tunable physicochemical properties and patient-specific performances (Shokouhimehr et al. 2021). Macroporosity was thus conferred to bioaerogels in 3D-printed alginate-hydroxyapatite aerogel scaffolds resulting in excellent cyto- and hemocompatibility, bioactivity, and stable integrity (Iglesias-Mejuto and García-González 2022). The dual processing strategy used in that case combined the advantages of supercritical fluid technology, such as the nanostructuration of aerogels, with the customization related to the 3D-printed constructs (Iglesias-Mejuto and García-González 2021). The technological combination provides a materials processing solution aligned with circular economy principles since it minimizes waste production and valorizes a residue ($scCO_2$). This environmentally friendly approach can be further endorsed if raw materials from sustainable sources are used (Tang et al. 2019). Different bioaerogel composites such as silk fibroin/cellulose or gelatin/collagen have been studied for bone tissue engineering but so far, only silk fibroin and alginate-based aerogels have been successfully manufactured by 3D-printing for bone regeneration purposes (Karamat-Ullah et al. 2021; Iglesias-Mejuto and García-González 2021, 2022; Ng et al. 2022; Al-Jawuschi et al. 2023).

Cellulose aerogels, also known as the third generation of aerogels, have demonstrated outstanding potential for bone tissue regeneration (Chen et al. 2021; Zhang et al. 2023). Namely, MC is a biocompatible polymer with high affinity to water, resulting in highly viscous solutions with shear-thinning behavior, a key factor for 3D-printing (Ahlfeld et al. 2020; Iglesias-Mejuto et al. 2024). The outstanding printability of MC-based inks results in end structures with a well-defined shape, following the initial CAD design and suitable for personalized medicine. Bacterial cellulose (BC) is another important cellulosic material with attractive properties for biomedical applications (Mbituyimana et al. 2021; Manan et al. 2022). Among those, BC has high crystallinity, high purity, excellent ability to retain water, and favorable mechanical performance. BC constitutes low-density

hydrogels composed of nanocellulose fibrils (NF) secreted by bacteria like *Komagataeibacter xylinus* (Roig-Sanchez et al. 2021) from low molecular weight carbon sources, free of lignin and hemicellulose (Zhang et al. 2023). Nevertheless, the tight arrangement of BC nanofibers (NF) results in low printability when employed as the main component of 3D-printing inks (Wang et al. 2021). Consequently, BC-NF have been successfully used with other polymers and nanomaterials as artificial scaffolds with enhanced mechanical performance (Mbituyimana et al. 2021; Roig-Sanchez et al. 2022). MC polymer was also successfully employed to prevent the delamination and aggregation of nanocellulose (Zhang et al. 2023). Furthermore, BC-metal oxide hybrid nanomaterials have been synthesized to improve the physicochemical characteristics of BC (Oun et al. 2020; Roig-Sanchez et al. 2021). Specifically, biocompatible superparamagnetic iron oxide nanoparticles (SPIONs) are one of the most prominent nanostructures, often incorporated into biomaterials to endow them with magnetic capability while enhancing their stability in physiological fluids for different tissue engineering applications (Pankhurst et al. 2003; Chiang et al. 2013; Charoensuk et al. 2016; Mortimer and Wright 2017; Singh et al. 2020; Luque-Michel et al. 2021). SPIONs have also demonstrated to improve scaffold functionality and mechanical performance (Charoensuk et al. 2016), to confer anti-biofilm (Gholami et al. 2019) and bacteriostatic properties (Shokouhimehr et al. 2021), to improve in vivo imaging (Hu et al. 2018) and to elicit bone repair in tissue engineering (Mortimer and Wright 2017).

The hypothesis of our work is that a new combination of MC and BC-NF in one single structure is feasible via a dual processing strategy comprising 3D-printing and supercritical fluid technologies and that the resulting cellulose-in-cellulose aerogels would have an enhanced structural resolution with high printing fidelities. Moreover, the use of BC-NF doped with SPIONs and blended with MC as aqueous inks to 3D-print gels should not modify the safety of the structures in terms of cell toxicity and hemolytic activity. After the 3D-printing of the wet gels, $scCO_2$ drying was then employed to obtain the aerogels. The printability by rheological assays and the morphological properties by nitrogen adsorption–desorption tests, confocal, SEM and TEM microscopies were used to assess the morphological and textural characteristics of the cellulose-in-cellulose 3D-printed aerogels. The magnetic performance of SPIONs-doped cellulose-in-cellulose aerogels was explored in view of potential tissue engineering applications. Bio- and hemocompatibility by in vitro and *in ovo* Hen's egg tests on the chorioallantoic membrane (HET-CAM) and a preliminary in vivo safety assessment based on *Artemia salina* were also carried out to unveil the biological performance of the scaffolds.

Materials and methods

Materials

Methylcellulose (MC, viscosity 15 cps, Mw 14 kDa, DS 1.5–1.9), citric acid monohydrate ($C_6H_8O_7{\cdot}H_2O$), NaOH, iron (III) acetylacetonate ($Fe(acac)_3$, 97%), titanium (IV) butoxide (TBOT, 97%), oleyamine (OA, 70%), polyvinylpyrrolidone (PVP, Mw 10 kDa) were supplied by Sigma-Aldrich (Steinheim, Germany). CO_2 (purity > 99.9%) was provided by Nippon Gases (Madrid, Spain) and absolute ethanol (EtOH) by VWR (Radnor, PA, USA). Water was purified by reverse osmosis (resistivity > 18 MΩ·cm; Milli-Q, Millipore®, Madrid, Spain).

K. xylinus bacterial strain (NCIMB 5346) was supplied by the Spanish Type Culture Collection (CECT, Spain) and Hestrin-Schramm (HS) culture medium was prepared with dextrose, peptone, yeast extract by Condalab (Madrid, Spain), and sodium phosphate dodecahydrate, and citric acid monohydrate. Sodium hydroxide (NaOH) at 0.1 M was used for cleaning BC pellicles. *A. salina* eggs and artificial sea water salt for artemia growth were purchased from JBL GmbH and Co., KG (Neuhofen, Germany).

Preparation of BC-NF and SPIONs doped BC-NF

Komagataeibacter xylinus was grown in 5 mL of HS culture medium and incubated statically for 7 days at 30 °C (Mira-Cuenca et al. 2021). 4 mL of bacterial broth was mixed with 56 mL of fresh HS medium and incubated at 30 °C for 5 days. BC pellicles were obtained, and posteriorly cleaned by immersion in 50% EtOH for 10 min, followed by two boiling steps in Milli-Q water for 20 min and twice in 0.1 M NaOH at 90 °C for 20 min. BC films were washed until pH was neutralized, and autoclaved in Milli-Q water at

121 °C for 30 min. Finally, BC pellicles were blended in 1 L of Milli-Q water for 10 min at the maximum speed of a commercial household blender (Jata electro Mod. BT1200, Tudela, Spain), obtaining BC-NF, which were then filtered with a Stericup Quick Release Filter Millipore with a PES membrane of 0.22 µm, autoclaved (121 °C, 30 min) and dispersed at 12 mg/mL in Milli-Q water.

BC-NF doped with SPIONs were synthesized by mixing 15 g of never-dried BC-NF with 40 mL of benzyl alcohol and 1100 mg of $Fe(acac)_3$ in a microwave vessel. After overnight incubation to allow the homogenization of reagents, the mixture was heated for 5 min at 60 °C (300 W) and 10 min at 210 °C (750 W) in a microwave oven (advanced flexible microwave synthesis platform from Milestone, Sorisole, Italy) operating at a frequency of 2.45 GHz and a maximum power of 750 W and 5% agitation. Finally, BC-NF decorated with SPIONs were cooled down, filtered, cleaned twice with acetone and once with Milli-Q water, and autoclaved (121 °C for 20 min). The obtained solution was composed of BC-NF decorated with SPIONs and some unbonded SPIONs.

3D-printing of cellulose-in-cellulose hydrogels

Aqueous 12 wt.% MC inks were firstly prepared, and then BC-NF suspensions (0.5, 1, 10, and 20 vol.%) doped or not with SPIONs were added to the MC inks under vigorous agitation (600 rpm) with a homogenizer (VWR vos 60, Radnor, PA, USA) for 1 h at room temperature (RT). Inks were degassed for 10 min in a sonication bath (Branson 3510 Emerson, Ferguson, MO, USA) to eliminate air bubbles. 3D-printed hydrogels were obtained with a Cellink BIOX Bioprinter (Boston, MA, USA) employing an extrusion printhead at 40 °C, 40 kPa and 3 mm/s, a 3-mL syringe, and a 410-µm nozzle. The resulting hydrogels had dimensions of 20×20×3 mm, a grid pattern, and 8 layers. Scaffolds were immersed in ethanol after the printing process to obtain alcogels.

Rheological evaluation of aqueous cellulose-in-cellulose inks

Flow behavior of the inks was recorded between 0.05 and 200 rad/s, at 20 °C and at 40 °C. Rheolyst AR-1000N rheometer (TA Instruments, Newcastle, UK) equipped with a Peltier plate and a cone geometry (40 mm diameter, 2°) with a solvent trap was employed. At least four replicates were evaluated for each ink formulation. The Eq. (1) (power law mathematical regression model) was fitted to the linear region of the viscosity vs shear rate-curves.

$$\eta = b\gamma^{c} \quad (1)$$

where η is the viscosity, b and c are the shear-thinning coefficients (consistency and flow indices, respectively) and γ is the shear rate.

$scCO_2$ drying of cellulose-in-cellulose alcogels

Alcogels were immersed in EtOH and placed into a 100-mL stainless steel autoclave (Thar Process, Pittsburg, PA, USA). A CO_2 flow (6 g/min) was supplied to the autoclave at 120 bar and 40 °C for 4 h. After CO_2 depressurization at a constant rate of 2 bar/min, aerogels were collected and stored at RT for further analysis. Aerogels were denoted as MC NF*x*-*y*; being *x* the content of BC-NF in the ink (0.5, 1, 10 or 20 vol.%), and *y* the concentration of the BC-NF suspension added (6 or 12 mg/mL) (Table 1). Aerogel formulations manufactured with BC-NF doped with SPIONs were indicated by the suffix *S*. Aerogels prepared only with MC (i.e. without BC-NF) were obtained as controls and simply denoted as MC. Alternatively, hydrogel precursors were submitted to freeze drying (−80 °C, vacuum) to obtain cryogels or to traditional

Table 1 Cellulose-in-cellulose aerogel formulations studied. At least 6 replicates were used per aerogel formulation

Aerogels	Ink composition			
	MC (wt.%)	NF (vol.%)	NF (mg/mL)	SPIONs
MC	12	–	–	–
MC NF0.5-6	12	0.5	6	–
MC NF1-6	12	1	6	–
MC NF10-6	12	10	6	–
MC NF20-6	12	20	6	–
MC NF0.5-6 S	12	0.5	6	Yes
MC NF1-6 S	12	1	6	Yes
MC NF10-6 S	12	10	6	Yes
MC NF0.5-12 S	12	0.5	12	Yes
MC NF1-12 S	12	1	12	Yes
MC NF10-12 S	12	10	12	Yes

evaporative drying methods (ambient drying at RT or oven drying at 37 °C) to obtain xerogels to compare the different gel drying methods. Finally, a thaw test was performed as reported elsewhere (Roig-Sanchez et al. 2022). Consistently, hydrogels were frozen in liquid nitrogen and thawed at RT to study the preservation of the macroscopical robustness.

Physicochemical characterization of MC aerogels

The skeletal density of aerogels (ρ_{skel}) was obtained at RT and 1.01 bar using a helium pycnometer (Quantachrome, Boynton Beach, FL, USA) and measuring five replicates. Apparent density (ρ_{app}) was calculated from Eq. (2), while scaffold porosity (ε) was determined employing Eq. (3). Volume shrinkage was also determined from the external dimensions of the structures before and after $scCO_2$ drying following Eq. (4):

$$\rho_{app} = \text{aerogel mass/aerogel volume} \tag{2}$$

$$\varepsilon(\%) = [1 - (\rho_{app}/\rho_{skel})] \times 100 \tag{3}$$

$$\begin{aligned}&\text{Volume shrinkage (\%)}\\ &= \left[(\text{alcogel volume} - \text{aerogel volume})/\text{alcogel volume}\right]\\ &\quad \times 100\ \text{Volume shrinkage (\%)}\\ &= \left[(\text{alcogel volume} - \text{aerogel volume})/\text{alcogel volume}\right]\\ &\quad \times 100\end{aligned} \tag{4}$$

Low-temperature N_2 adsorption–desorption analysis (ASAP 2000 Micromeritics Inc.; Norcross, GA, USA) was used to determine the textural parameters of the scaffolds. Aerogel samples were degassed under vacuum at RT for 24 h. Specific surface area (A_{BET}) of samples was obtained by the BET (Brunauer–Emmett–Teller) method. Specific pore volume (V_p), pore size distribution and mean pore diameter (d_p) were calculated by BJH (Barrett–Joyner–Halenda) method from the desorption branch of the isotherm. Morphology of aerogels was analyzed by scanning and transmission electron microscopy (SEM, EVO LS15, Zeiss, Oberkochen, Germany; TEM, JEOL JEM-2010, JEOL, Tokyo, Japan -operating at 200 kV-). Aerogels were iridium-sputtered before being imaged by SEM, whereas phosphotungstic acid (aqueous 1%) was used as the staining solution of aerogels before TEM analysis. SEM–EDX and mapping of the chemical elements present in the aerogel scaffolds were also performed. Confocal microscopy was used to evaluate the distribution of BC-NF decorated with SPIONs in the aerogel matrix with a Leica TCS-SP2 spectral confocal microscope (Leica TCS-SP2, Leica Microsystems Heidelberg GmbH, Manheim, Germany) in the 405-561 nm range. Magnetic response of SPIONs trapped in aerogels was studied by Superconducting Quantum Interface Device analysis (SQUID). Aerogels (0.5×0.5×0.3 cm) were placed in a plastic tube. Magnetization vs applied magnetic field was obtained in the -6/6 T range at 5 K (Quantum Design MPMS-3, VSM mode). Water contact angle was determined to evaluate the effect of SPIONs incorporation on the surface hydrophilicity. 9 µL of Milli-Q water were deposited on the surface of the aerogel scaffolds and the drop shape was recorded. The water contact angle was obtained using ImageJ software (2 measurements per replicate, 4 replicates per formulation). 4-month stability analysis of aerogels was performed by N_2 adsorption–desorption and SEM analysis after conservation of the structures at RT, protected from light and stored in closed plastic jars.

Printing fidelity tests

Shape fidelity factor (SFF) for alcogels and aerogels was calculated from Eq. (5). For SPIONs doped samples, further fidelity indexes (α, L, D, A) were calculated from Eqs. (6) to (9) (Theus et al. 2022).

$$\text{SFF} = \text{alcogel or aerogel printed area/CAD area (printing file)} \tag{5}$$

$$\alpha = \text{angle between printed strands/designed angle between printed strands} \tag{6}$$

$$\text{L} = \text{length of printed strand/length of designed strand} \tag{7}$$

$$\text{D} = \text{diameter of printed strand/diameter of designed strand} \tag{8}$$

$$\text{A} = \text{area between printed strands/designed area between printed strands} \tag{9}$$

Cytocompatibility tests

The resazurin (Sigma-Aldrich) conversion into resorufin by metabolically active cells was used to assess the cytocompatibility of aerogels.

Viability after 24 and 72 h of mouse embryo fibroblasts (NIH/3T3) in contact with aerogels was evaluated. Cells at concentration of 12,000 cells/cm^2 were seeded in 24-well plates with 600 µL of Dulbecco's Modified Eagle's Medium growth media supplemented with 10% bovine calf serum, penicillin 100 U/mL and streptomycin 100 g/mL and were incubated at 37 °C in a humidified atmosphere enriched with 5% CO_2. Aerogels (0.5 × 0.5 × 0.3 cm) were UV-sterilized for 30 min and placed in culture inserts. After 24 and 72 h of culture, scaffolds were removed, the growth medium was aspirated and 100 µL of 44 µM resazurin in fresh growth medium was added into each well. Resazurin solution alone was used as a blank. After 3 h of incubation under the same conditions, fluorescence was measured at an excitation wavelength of 544 nm and emission wavelength of 590 nm in a microplate reader (Infinite® M200, Tecan Group Ltd., Männedorf, Switzerland). Cells in the absence of aerogels were maintained at the same conditions to be used as positive controls and cells in contact with cisplatin 10 µM were used as negative controls. All tests were run in triplicate.

Hemolytic activity test

The hemolytic activity of aerogels was assessed using human blood (Galician Transfusion Center, Spain) obtained in accordance with the Declaration of Helsinki. Fresh human blood was diluted to 3% (v/v) in 0.9% (w/v) NaCl. 1 mL of diluted blood was transferred to Eppendorf tubes containing the aerogels (0.5 × 0.5 × 0.3 cm), 100 µL of 4% (v/v) Triton X-100 (positive control) or 100 µL of phosphate buffer saline (PBS, pH 7.4; negative control). Tests were carried out in triplicate. Samples were incubated for 60 min at 37 °C and 100 rpm and centrifuged at 10,000*g* for 10 min (Sigma 2-16P, Sigma Laboratory Centrifuges, Osterode am Harz, Germany). 150 µL of supernatant were transferred to a 96-well plate, and the absorbance of the haemoglobin was measured at λ = 540 nm (FLUOStar Optima, BMG Labtech, Ortenberg, Germany). Hemolysis was determined by Eq. (10):

$$\text{Hemolysis}\ (\%) = \left(\text{Abs}_s - \text{Abs}_n\right)/\left(\text{Abs}_p - \text{Abs}_n\right) \times 100 \quad (10)$$

Abs_s is the absorbance of samples with aerogels, Abs_n is the negative control absorbance (0% of hemolysis), and Abs_p is the positive control absorbance (100% of hemolysis).

HET-CAM test

Aerogels were evaluated by a HET-CAM (hen's egg-chorioallantoic membrane) test according to Interagency Coordinating Committee on the Validation of Alternative Methods (ICCVAM) guidelines (2010; Salerno et al. 2017). Fertilized hens' eggs (50–60 g, Coren, Ourense, Spain) were used after incubation at 37 °C in a 60% humidified atmosphere with an 8 h scheduled rotation (incubator Ineltec CC SR 0150, Barcelona, Spain). On day 9, a small window was opened to access the CAM and aerogels (0.5 × 0.5 × 0.3 cm) were placed there. 300 µL of 0.1 N NaOH or PBS pH 7.4 were put in contact with CAM as positive and negative controls, respectively. Each test was carried out in duplicate, and vessels of CAM were observed for 5 min after aerogels contact to evaluate the appearance of haemorrhage, vascular lysis, clotting, hyperemia, or changes in small vessel diameter of CAM by visual inspection.

Preliminary safety tests

The safety of aerogels was evaluated by measuring the mortality of *A. salina* as a preliminary in vivo model (Hamidi et al. 2014; Ferreira-Gonçalves et al. 2022). Commercial seawater salt was dissolved in tap water according to supplier instructions, and *A. salina* eggs were left to hatch at 25–30 °C for 48 h, under aeration and illumination. 1 mL of seawater with 10–15 nauplii was transferred to a 24-well plate using six replicates per formulation. 100 µL of seawater salt was used as negative control and 100 µL of DMSO 100% was used as positive control. Nauplii in contact with aerogels (0.5 × 0.5 × 0.3 cm) were incubated for 24 h under the same conditions. Mortality was then calculated according to Eq. (11). 100 µL of DMSO 100% was added to kill the remaining alive nauplii.

$$\text{Mortality}\ (\%) = (\text{Dead 24 h}/\text{Dead Total}) \times 100 \quad (11)$$

Dead 24 h is the number of dead nauplii after 24 h of contact with aerogels and Dead Total is the total number of nauplii per well, as counted in a magnifying glass.

$scCO_2$ sterilization of aerogels

Aerogels were placed into thermally sealed sterilization pouches in a high-pressure 600-mL autoclave (NovaGenesis, NovaSterilis Inc., Ithaca, NY, USA). 1200 ppm of H_2O_2 were introduced into the autoclave before pressurization with CO_2 until 100 bar at 40 °C. After 30 min contact time, the autoclave was depressurized at 5 bar/min. The texture and morphology of the sterilized aerogels were compared with the unsterilized formulations. Sterilized aerogel formulations were denoted with the *-st* suffix.

Statistical analysis

Results were reported as mean value ± standard deviation and post hoc Tukey HSD multiple comparison tests were performed to determine the statistical significance of differences between formulations concerning controls. Values of $p < 0.05$ were considered statistically significant.

Results and discussion

Aerogel processing and printing fidelity assessment

Different nanocellulose-based biomaterials have previously displayed good printability and shear-thinning behavior under the applied pressures required for 3D-printing (Athukoralalage et al. 2019). Cellulose-in-cellulose inks were homogeneously obtained with different proportions of BC-NF (Table 1). 3D-printing was performed without relevant clogging of the nozzle for the different formulations studied, thus allowing the incorporation of BC-NF concentrations as high as 20 vol.%. The rheological properties of the inks were analyzed by studying their viscosity *versus* shear rate sweep, simulating the extrusion-based 3D-printing process by rotational rheology (Corker et al. 2019). Shear-thinning behavior was observed for all the formulations regardless the presence of SPIONs or the experimental temperature (Fig. 1a). Higher viscosities were reached at higher printing temperatures (40 °C) for all the formulations studied. This observation is coherent with the MC gelation at temperatures above RT, due to the MC thermal-responsiveness behavior (Cochis et al. 2018; Shin et al. 2020). The herein obtained shear-thinning effect was less accused in the case of pure MC inks and reached the highest viscosities for those inks containing the highest BC-NF concentration (MC NF10-12 S). A tighter arrangement of the BC-NF could explain this observation, which could increase the ink's viscosity when the BC-NF concentration rises. Furthermore, pseudoplastic behavior was displayed for all formulations tested (Fig. 1b), as non-linear

Table 2 Shear-thinning coefficient values of inks calculated through power law model

Aerogel formulations	20 °C		40 °C	
	b	c	b	c
MC	6.95	0.80	61.74	0.43
MC NF10-12 S	9.20	0.76	49.98	0.38

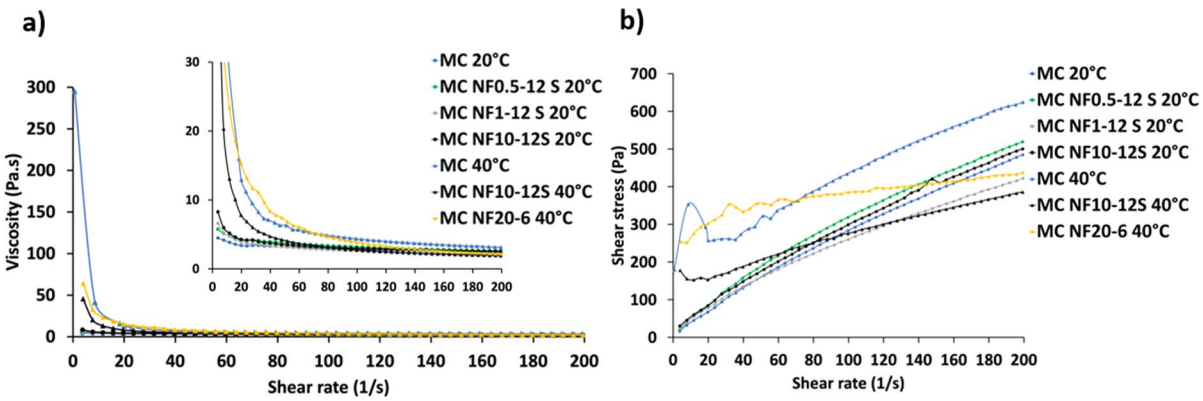

Fig. 1 Rheological characteristics of different ink formulations by **a** overall viscosity variation with respect to the shear rate and **b** shear stress with respect to shear rate

behavior was observed between shear stress and shear rate especially at 40 °C.

Rheological measurements were fitted to the power law equation (Eq. 1). c values closer to zero (Table 2) were obtained when rheology experiments were performed at 40 °C than at 20 °C, thus suggesting a more pronounced shear-thinning behavior and consequently, a better performance for extrusion-based 3D-printing. Regarding b values, results show higher extrudability at lower temperature for both formulations, maybe due to the lower viscosities achieved by MC at lower temperatures (Fig. 1a).

The 3D-printed gel scaffolds were firstly immersed in ethanol to obtain an alcogel, aerogel scaffolds were then produced after the supercritical drying of the alcogels. The overall process was evaluated regarding its reproducibility (Fig. 2a–d). Aerogels showed typical volume shrinkage values (50–60%) for bioaerogels with no relevant differences between the aerogel formulations loaded and unloaded with BC-NF (Fig. 2a). SFF values of alcogels and aerogels were determined to study the printing fidelity. Alcogels loaded with different concentrations of BC-NF displayed similar SFF values while aerogels displayed higher SFF values at the highest BC-NF concentrations (Fig. 2b). Volume shrinkage of gels loaded with BC-NF and SPIONs was lower at the highest concentration of BC-NF, showing a significant decreasing tendency with increasing concentration of BC-NF doped with SPIONs (Fig. 2c). The presence of the nanofibers may split the total volume of the gel into interfibrillar subregions limiting the processing stresses and thus hindering the shrinkage of the gel (Linhares et al. 2019). In general, the presence of BC-NF in the aerogel scaffolds resulted in a better-defined 3D-printed pattern with respect to their non-BC-NF loaded counterparts. An enhancement in the printing fidelity was also observed due to the incorporation of increasing concentration of BC-NF doped with SPIONs into the aerogel structure (Fig. 2d). BC-NF also promoted shape fidelity and enhanced the reinforcement and 3D-printing resolution in silk fibroin scaffolds (Huang et al. 2019). Similar SFF values were herein obtained with and without SPIONs, thus suggesting that the incorporation of SPIONs is not causing any negative impact on the printing fidelity of aerogels (Fig. 2b vs. d).

The scaffolds containing BC-NF doped with SPIONs were selected for a complete printability study and further fidelity indexes were calculated (Fig. 2e). Angles and diameter of strands of scaffolds were printed with a high fidelity as compared to their computer-designed counterparts for all formulations with values close to one for α and D indexes. Area (A) and length (L) indexes of the aerogels were lower than 0.4 and 0.7 respectively, due to the volume shrinkage of the 3D-printed gel after supercritical drying, showing the best values at intermediate concentrations of BC-NF doped with SPIONs.

Contact angle measurements have a strong correlation with the wettability of the surfaces (García-González et al. 2009). Higher contact angles were obtained in aerogel surfaces when SPIONs were incorporated (Fig. 2f), possibly due to an increment in the surface roughness and in the hydrophobic behavior. Similar behavior were described for gelatin-based materials when iron oxide nanoparticles were incorporated (Drobota et al. 2022) and silk-fibroin NF doped with SPIONs incorporated into scaffolds (Nazari et al. 2020).

Physicochemical characterization of cellulose-in-cellulose aerogels

Hierarchical porous MC aerogels with an open and interconnected porosity of different scale sizes were fabricated with and without BC-NF (Fig. 3). Visual observation of the aerogel formulations unveiled 3D-grid patterns with open macroporosities (Fig. 3, inserts). The highest structural resolution in visual appearance was observed for aerogels containing the highest amount of BC-NF (Fig. 3e vs a, c). The porosity of MC aerogels (ε in Table 3) was close to the previously reported nanocellulose synthesized by a similar procedure (Zeng et al. 2014). All aerogel formulations presented meso- and macropores within the filaments, but larger macropores were observed when BC-NF were incorporated (Fig. 3d, f vs. b). Macropores are essential for tissue engineering applications, specifically, the presence of pores between 10 and 20 µm were related to cell infiltration (Huang et al. 2019), as the herein observed inside the printed filaments when BC-NF were incorporated into aerogels. Macropores between 100 and 600 µm found between printed strands are linked to good nutrient supply. The open porous and hierarchical structure with meso- and macropores of aerogels with BC-NF

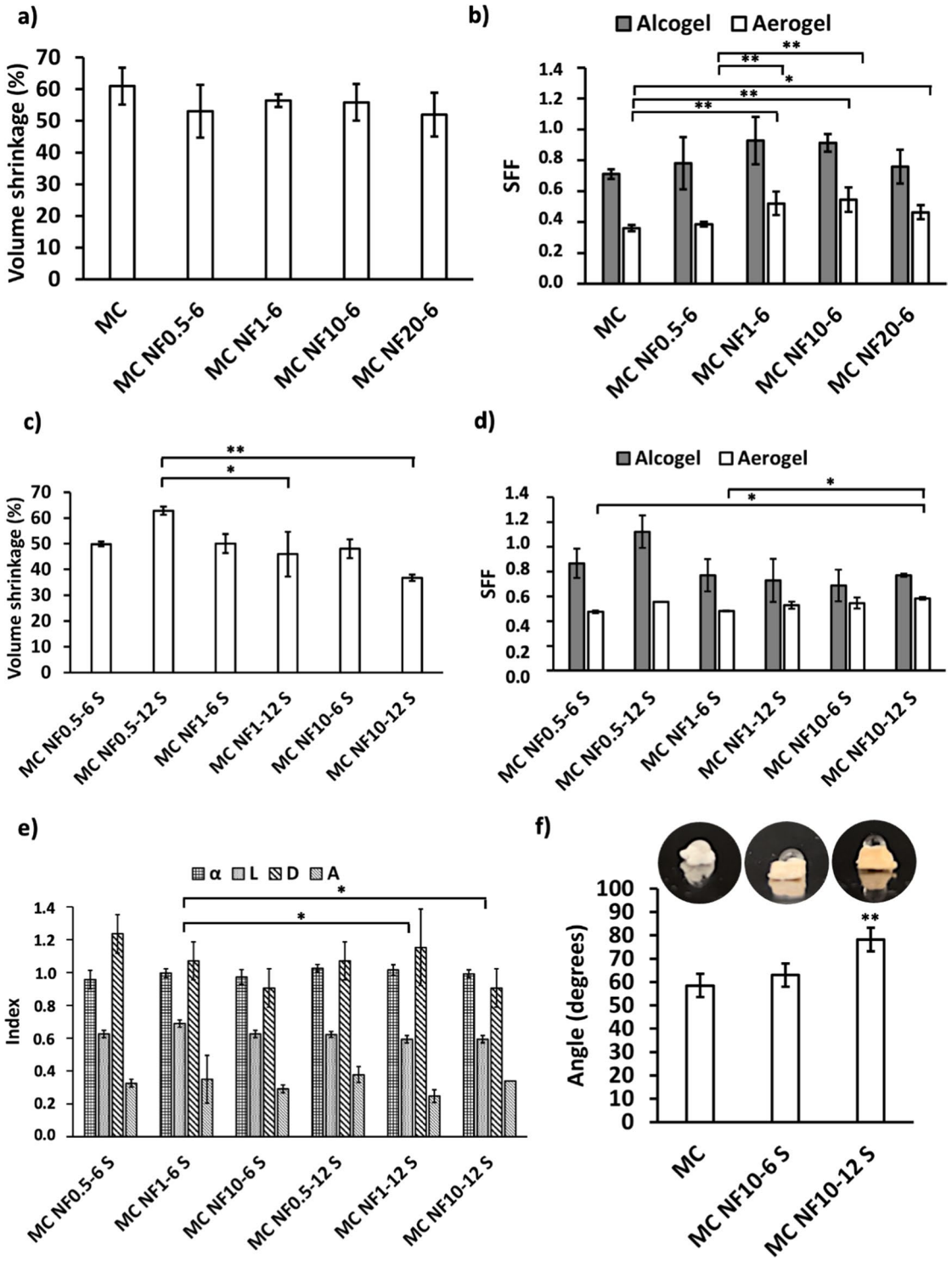

Fig. 2 Volume shrinkage (in percentage) and SFF of different MC aerogels prepared with increasing concentrations of BC-NF (0–20 vol.%) **a, b** without or **c, d** with SPIONs. **e** Different printing fidelity indexes (α, L, D, A) and **f** contact angle measurements for different formulations of aerogels decorated with SPIONs. Significant differences among groups were represented as * or ** (post hoc Tukey HSD multiple comparison test, $p < 0.05$ or $p < 0.01$, respectively)

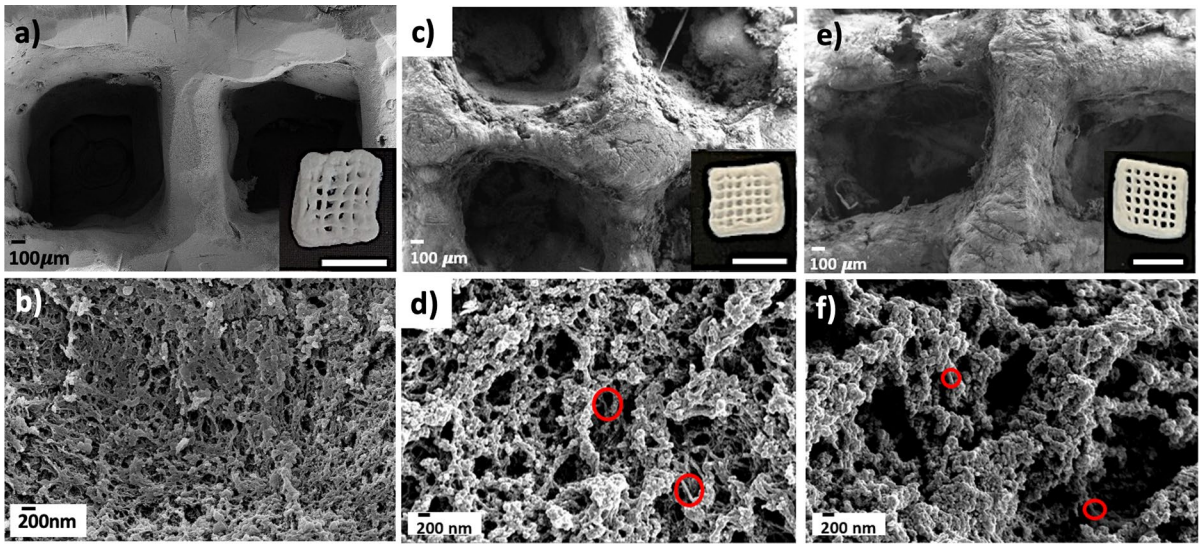

Fig. 3 SEM pictures of cellulose-in-cellulose aerogels: **a, b** MC; **c, d** MC NF0.5–6 and **e, f** MC NF20-6. Aerogels imaged at two different magnifications. Inserts in (**a, c, e**): visual appearance of the aerogel scaffolds (scale bar: 1 cm). Red circles represent zones where the presence of BC-NF was detected by visual inspection

Table 3 Textural properties of cellulose-in-cellulose aerogels

Aerogel scaffold	A_{BET} (m^2/g)	d_p (nm)	V_p (cm^3/g)	ρ_{app} (g/cm^3)	ρ_{skel} (g/cm^3)	ε (%)
MC	268 ± 13	19 ± 1	1.71 ± 0.09	0.18 ± 0.04[a]	1.35 ± 0.03	87 ± 3
MC NF0.5-6	241 ± 12	22 ± 1	1.77 ± 0.09	0.19 ± 0.03[a]	1.27 ± 0.03	85 ± 2
MC NF1-6	237 ± 12	22 ± 1	1.75 ± 0.09	0.12 ± 0.02[b]	1.12 ± 0.03	83 ± 2
MC NF10-6	256 ± 13	21 ± 1	1.83 ± 0.09	0.13 ± 0.02[b]	1.23 ± 0.03	84 ± 2
MC NF20-6	283 ± 14	25 ± 1	2.37 ± 0.12	0.13 ± 0.01[b]	1.22 ± 0.02	84 ± 2
MC st	171 ± 9	17 ± 1	1.04 ± 0.05	0.19 ± 0.01	1.45 ± 0.02	85 ± 1
MC NF0.5-6 st	154 ± 8	19 ± 1	1.00 ± 0.05	0.22 ± 0.01	1.30 ± 0.09	83 ± 1
MC NF1-6 st	188 ± 9	20 ± 1	1.25 ± 0.06	0.23 ± 0.03	1.16 ± 0.02	80 ± 2
MC NF10-6 st	197 ± 10	17 ± 1	1.13 ± 0.06	0.20 ± 0.03	1.27 ± 0.02	84 ± 2
MC NF20-6 st	238 ± 12	23 ± 1	1.76 ± 0.09	0.18 ± 0.02	0.80 ± 0.08	77 ± 3

Equal letter (a or b) denotes statistically homogeneous group (ANOVA Tukey's test, $p < 0.05$). Notation: st: $scCO_2$ sterilized samples, A_{BET}: specific BET surface area, d_p: BJH-mean pore diameter, V_p: BJH-specific pore volume, ρ_{app}: apparent density, ρ_{skel}: skeletal density, ε: porosity

(Fig. 3d, f), was previously associated with BC-NF based biomaterials (Zeng et al. 2014).

Similar porosity (80–85%) was obtained for the different aerogel formulations studied (Table 3). Similar values (80%) were also reported for BC-NF scaffolds (Panaitescu et al. 2022). The tight arrangement described for BC-NF may help maintain the aerogel structure without modifying their porosity. The apparent density of the aerogels significantly changed when BC-NF were incorporated into the scaffolds once a threshold BC-NF concentration value (above 0.5 vol.%) was used. These results are coherent with the observed decreasing tendency in volume shrinkage of gels when BC-NF were incorporated at higher concentration (12 mg/mL) and in higher volumes (0.5 vs 1–10 vol. %) (Fig. 2c). The increase in mass with the addition of the nanofibers was compensated by the lower shrinkage in volume of the gels resulting in lower apparent densities of aerogels, as similarly reported for certain fiber-reinforced aerogels in the literature (Linhares et al. 2019).

The specific surface area and pore volume were similar for all the formulations studied, suggesting that incorporating BC-NF into the structures did not have any detrimental effect on the textural properties of the aerogels. Indeed, an important increase in the specific pore volume of ca. 35% was observed for the scaffolds with the highest concentration of BC-NF. Similar BET surface area (241 m^2/g) and interconnected nanostructure were described for BC-NF loaded glass scaffolds, but with lower pore volumes (0.33 cm^3/g) (Luo et al. 2017).

BC-NF decorated with SPIONs were homogeneously incorporated in the aerogel structures resulting in a change of color of the printed aerogels from white to orange when SPIONs were present. BC-NF doped with SPIONs were randomly distributed throughout the porous structure of the matrix (Fig. 4b, c) with similar nanofibrillar organization in the material to aerogels containing BC-NF without SPIONs (Fig. 4a) and to other scaffolds with BC-NF (Li et al. 2022). EDX spectra of the aerogels confirmed the presence of SPIONs in the scaffolds (Fig. 4). Accordingly, no Fe peaks were observed when SPIONs were not added (Fig. 4a), while these peaks appeared when SPIONs were incorporated at a low (Fig. 4b) or a high (Fig. 4c) concentration. Furthermore, the mapping of the chemical elements in the aerogels confirmed the presence of Fe homogeneously distributed throughout the aerogel structure due to SPIONs doping (Fig. 4d). SEM image of the zone where the mapping was performed shows also white granules that could be due to SPIONs aggregates in the scaffold, similarly to those previously described for pectin aerogels monoliths also loaded with iron oxide magnetic nanoparticles (García-González et al. 2012).

The presence of BC-NF in the aerogels and the preservation of their integrity after all the processing steps were also confirmed by TEM imaging (Fig. 4e, f), where the BC-NF had diameters very close to those measured by SEM imaging (42 ± 7 nm vs 46 ± 8 nm). SPIONs in aerogels (Fig. 4e, f) have a size and morphology coherent with previous measurements of SPIONs not incorporated into aerogels (12 ± 2 nm) thus indicating the stability of the nanoparticles after the dual processing strategy. Moreover, the stability of the SPIONs incorporated into the aerogels and their homogeneous distribution in the material were endorsed by confocal microscopy, where higher intensities were observed for the aerogel formulations with the highest amount of SPIONs (Fig. 4h) with respect to the ones with lower amount (Fig. 4i, j) or without SPIONs (Fig. 4g).

The dual porous structure of the 3D-printed structures was preserved for BC-NF doped SPIONs aerogels (Fig. 4b, c). No relevant differences were observed regarding the textural properties of different SPIONs-decorated aerogels (Table 4), thus suggesting the lack of effect of incorporating SPIONs in the aerogel structure. An important improvement in the BET surface area was herein reported with respect to previous magnetite aerogels obtained by supercritical drying (120 m^2/g) (Anastasova et al. 2022). The morphology of these aerogels can only be obtained when the supercritical drying method was used, regardless the selected printed pattern or external shape (Fig. 5a, b, c). Using other drying methods, the shape was not maintained (Fig. 5 d, e, f), and the textural parameters dramatically decreased after ambient, oven or freeze drying of hydrogel scaffolds (A_{BET} for cryogels and xerogels were below de detection limit, i.e. < 5 m^2/g). In the case of freeze-dried gels (i.e. cryogels), the interfibrillar macroporosity was lost and several cracks appeared along the structure (Fig. 5d). After ambient and oven dried gels, a dramatic volume shrinkage (*ca.* 90%) and, in the case of presence of SPIONs, a darker color were obtained (Fig. 5e, f). These results are coherent with those obtained for other polysaccharide cryogels and xerogels (López-Iglesias et al. 2019; Groult et al. 2021) and confirm that ambient, oven or freeze drying are inadequate methods to obtain the advanced textural performance essential for bone tissue engineering. Also, hydrogels were frozen in liquid nitrogen and thawed at RT. After freezing, only the external shape was preserved but not the 3D-printed pattern (Fig. 5g). Consequently, after thawing at RT the 3D-printed hydrogel did not return into their initial morphology (Fig. 5h), thus suggesting that this procedure was not adequate to preserve the robustness and the advanced 3D-printed structure. Hydrogels without an internal 3D-printed pattern have previously maintained their

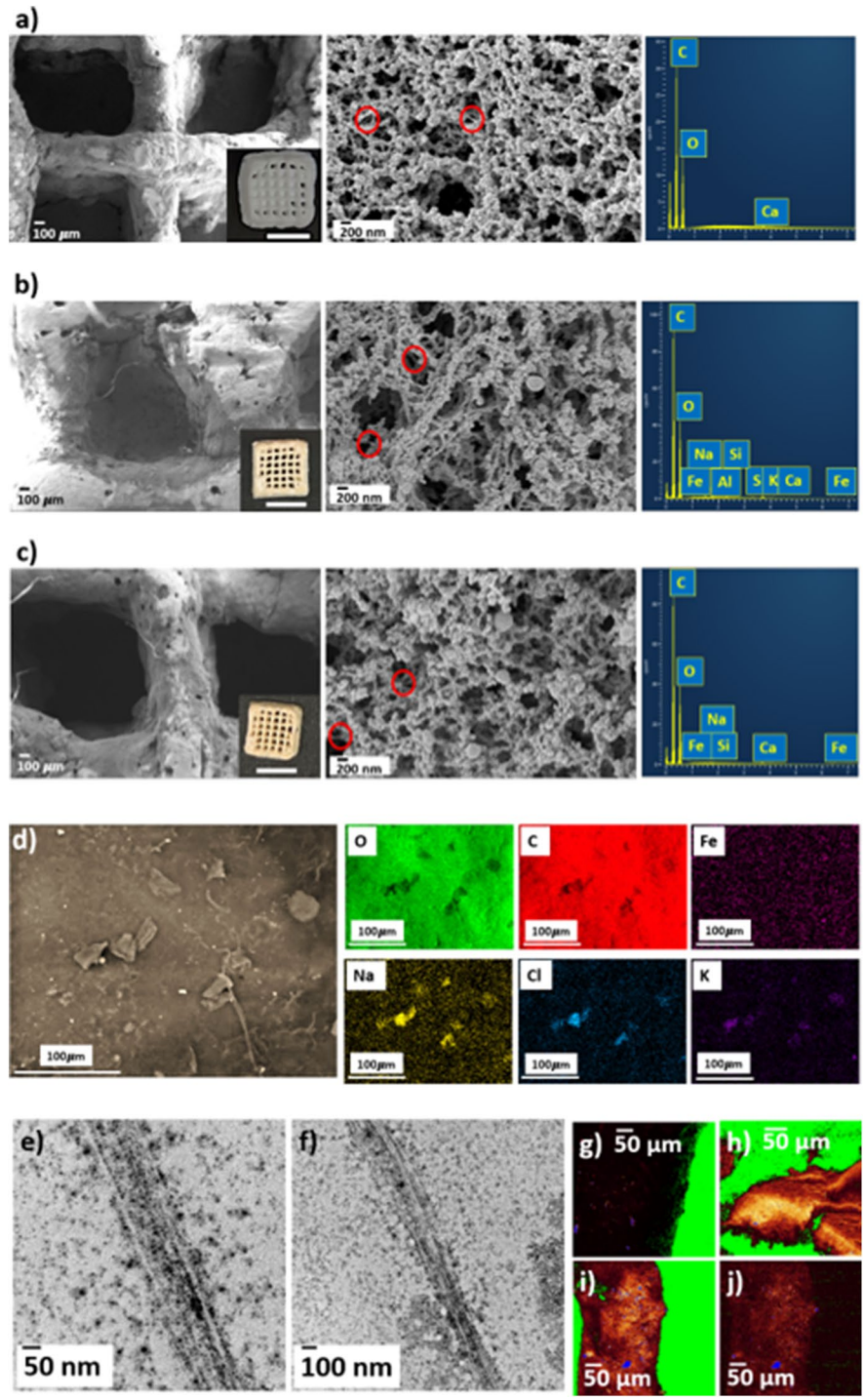

Fig. 4 SEM images (left and middle) and EDX spectra (right) of different cellulose-in-cellulose aerogels: **a** MC NF10-6 **b** MC NF10-6 S, and **c** MC NF10-12 S. **d** SEM image and mapping of the chemical elements present in MC NF10-12 S aerogels. Inserts: visual appearance of the aerogel scaffolds (scale bar: 1 cm). Red circles represent zones where the presence of BC-NF was detected by visual inspection. **e, f** TEM images of cellulose-in-cellulose aerogels (MC NF10-12 mg/mL S) observed at two different magnifications. Black dots in TEM images are probably due to the formation of SPIONs clusters and their accumulation in the aerogels. Confocal images of different cellulose-in-cellulose aerogels: **g** MC, **h** MC NF10-12 S observed at 405 nm, and **i,j** MC NF10-6 S observed at 405 and 488 nm

external shape after freezing in liquid nitrogen (Roig-Sanchez et al. 2022).

No relevant changes in terms of textural properties were observed after storage of different aerogel formulations in closed plastic jars for 4 months (Table 5). Moreover, the high structural resolution was preserved after this time period (Fig. 6a, c) as well as the dual porous structure with the BC-NF randomly distributed on it (Fig. 6b, d). All these results suggest the preliminary stability at RT of the 3D-printed cellulose-in-cellulose aerogels with and without SPIONs.

Magnetic properties of SPIONs decorated aerogels

SPIONs were not functionally affected by the 3D-printing or the $scCO_2$ processing as the normalized magnetization vs temperature plot of aerogel composites and of BC-NF doped with SPIONs had similar magnetization behavior (Fig. 7a). Zero-field cooled (ZFC) magnetization increases with temperature until it reached the blocking temperature ($T_B = 140$ K). Above this temperature, aerogels were superparamagnetic; below the blocking temperature, samples were ferrimagnetic (Fig. 7b). Remanent magnetization value (M_R) at 5 K was used to know the content of BC-NF doped with SPIONs in the aerogels. M_R of SPIONs was 30 emu/g at 5K (previous work). Accordingly, MC NF10-12 aerogels had 1.1 ± 0.1 wt.% of BC-NF labelled with SPIONs and 0.15 ± 0.02 wt.% of SPIONs. MC NF10-6 formulations had 0.42 ± 0.06 wt.% of BC-NF doped with SPIONs and 0.06 ± 0.01 wt.% of SPIONs. Similar results in terms of magnetic behavior were reported for pectin aerogels loaded with iron oxide magnetic nanoparticles (García-González et al. 2012). Further SPIONs contents should be incorporated into aerogel structure to confer magnetic properties at levels of relevance for biomedical applications.

Biocompatibility and preliminary safety tests

High viability of fibroblast cells assessed by resazurin test was obtained after 24 and 72 h in contact with cellulose-in-cellulose aerogels (Fig. 8a). However, no significant differences were observed in cell viabilities for the aerogels loaded with different BC-NF contents, thus indicating no negative impact of the BC-NF on cell survival. Nanocellulose has previously shown excellent biocompatibility and the ability to support cell growth in 3D-printed biomaterials (Athukoralalage et al. 2019). BC-NF composites have also been demonstrated to be biocompatible and able to promote cellular adhesion and proliferation of human mesenchymal stem cells (Jin et al. 2016).

Preliminary safety assays showed high viability of *A. salina* after 24 h of contact with aerogels loaded with different BC-NF concentrations (Fig. 8b) and these results endorse the previous ones. Aerogels doped with SPIONs also induced a neglectable mortality of *A. salina*, suggesting the preliminary safety of the BC-NF aerogels decorated with SPIONs. Similar results were reported for pectin aerogels (Ferreira-Gonçalves et al. 2022).

Biomaterials contact with blood is the first event in a bone wound after implantation, broadly affecting the subsequent bone healing (Lagadec et al. 2017). Moreover, bone defects are commonly associated with a damage to blood vessels in the surrounding tissue. The contact of implants with blood induces the formation of a blood clot and the recruitment of inflammatory cells, the first steps in bone regeneration (Yang et al. 2016). Consequently, studying interactions between host blood and biomaterials is crucial to ensure the hemostasis process (Shiu et al. 2014). No hemolytic activity was detected for the aerogels containing the highest concentration of NF doped with SPIONs, with significant differences to the positive control (Fig. 8c) and with similar results to magnetite-loaded aerogels (Anastasova et al. 2022). These results suggest the absence of hemolysis due to BC-NF-loaded aerogels, either with or without SPIONs. HET-CAM images obtained after the contact of SPIONs doped samples were in accordance with these results, with no hemorrhage detected by visual inspection (Fig. 8d). All these data indicate that the studied aerogel scaffolds triggered no lysis or coagulation phenomena of blood cells. These are

Table 4 Textural properties of cellulose-in-cellulose aerogels

Aerogel scaffold	A_{BET} (m^2/g)	d_p (nm)	V_p (cm^3/g)
MC NF0.5-6 S	229 ± 11	19 ± 1	1.49 ± 0.07
MC NF1-6 S	235 ± 12	21 ± 1	1.63 ± 0.08
MC NF10-6 S	250 ± 13	20 ± 1	1.65 ± 0.08
MC NF0.5-12 S	221 ± 11	19 ± 1	1.46 ± 0.07
MC NF1-12 S	245 ± 12	21 ± 1	1.71 ± 0.09
MC NF10-12 S	209 ± 11	19 ± 1	1.30 ± 0.07

Notation: A_{BET}: specific BET surface area, d_p: BJH-mean pore diameter, V_p: BJH-specific pore volume

good results since coatings like polyethylene glycol were needed to coat iron oxide nanoparticles before obtaining functionalized and biocompatible BC-NF (Arias et al. 2016). At the SPIONs concentrations herein employed, no coating of SPIONs was required to enhance their biocompatibility, maybe due to their inclusion inside the aerogel structure.

Sterility procedure evaluation

Different methods like gamma radiation or ethylene oxide are being used to sterilize biomaterials; most of these options were unsuitable for polymeric structures due to their negative impact on their physicochemical characteristics (Ahlfeld et al. 2020; Ribeiro et al. 2020). For this reason, $scCO_2$ is increasingly studied as a sterilizing agent able to preserve the physicochemical features of implants and achieve the sterility levels required for implantable medical devices (Santos-Rosales et al. 2019, 2021). After the sterilization procedure, no relevant morphological and textural changes on aerogels due to $scCO_2$ postprocessing were observed (Table 3). A similar porous structure (pore size distribution and morphology) was also observed for all the formulations studied, including the ones without BC-NF, by comparison of the SEM images obtained before (Fig. 1) and after the sterilization (Fig. 9). There was no statistical difference in

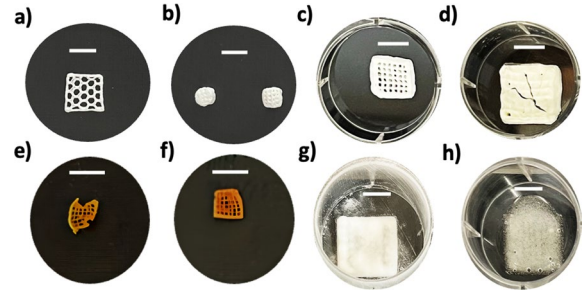

Fig. 5 Effect of drying method for MC-based formulations on the resulting MC-dried gels: **a, b, c** MC NF20-6 aerogel obtained after $scCO_2$ drying, **d** MC NF20-6 cryogel obtained after freeze drying, **e** MC NF10-6 S xerogel obtained after ambient drying at RT, and **f** MC NF10-6 S xerogel obtained after oven drying at 37 °C. **g** MC NF20-6 hydrogel just after freezing in liquid nitrogen. **h** MC NF20-6 hydrogel after thawing at RT. Scale bar: 1 cm

Table 5 Textural properties of cellulose-in-cellulose aerogels after 4 months of storage

Aerogel scaffold	A_{BET} (m^2/g)	d_p (nm)	V_p (cm^3/g)
MC	273 ± 14	18 ± 1	1.66 ± 0.08
MC NF0.5-6 S	164 ± 8	18 ± 1	1.01 ± 0.05
MC NF1-6 S	295 ± 15	19 ± 1	1.79 ± 0.09
MC NF10-6 S	229 ± 11	18 ± 1	1.35 ± 0.07
MC NF0.5-12 S	259 ± 13	14 ± 1	1.13 ± 0.06
MC NF1-12 S	230 ± 12	21 ± 1	1.57 ± 0.08
MC NF10-12 S	206 ± 10	21 ± 1	1.41 ± 0.07

Notation: A_{BET}: specific BET surface area, d_p: BJH-mean pore diameter, V_p: BJH-specific pore volume

the values of porosity of the aerogel scaffolds before and after the supercritical sterilization treatment (Table 3). The distribution and structure of BC-NF were preserved and intercalated in the porous aerogel structure after the $scCO_2$-assisted sterilization (Fig. 9, red circles).

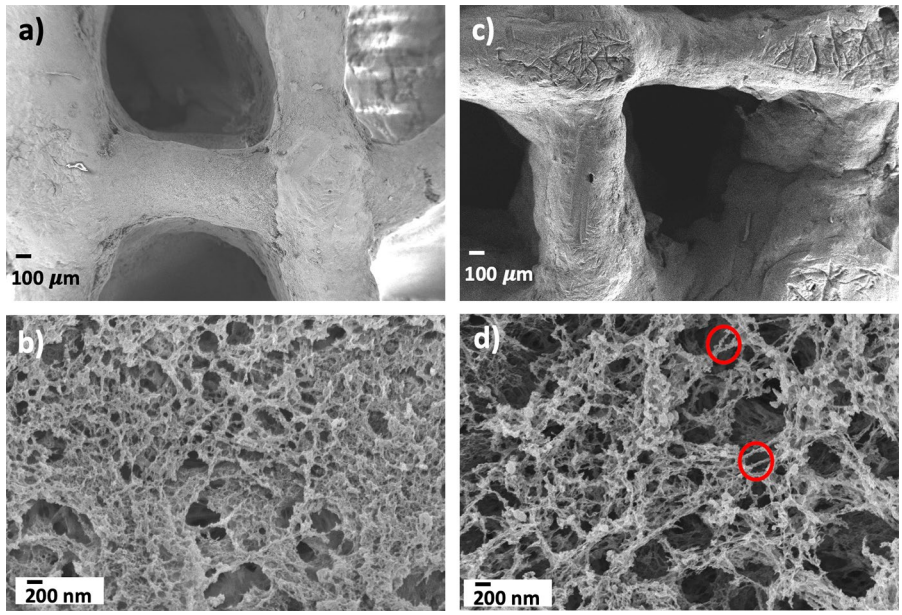

Fig. 6 SEM pictures of cellulose-in-cellulose aerogels after 4-month storage: **a, b** MC, and **c, d** MC NF10-6 S. Aerogels imaged at two different magnifications. Red circles represent zones where the presence of BC-NF was detected by visual inspection

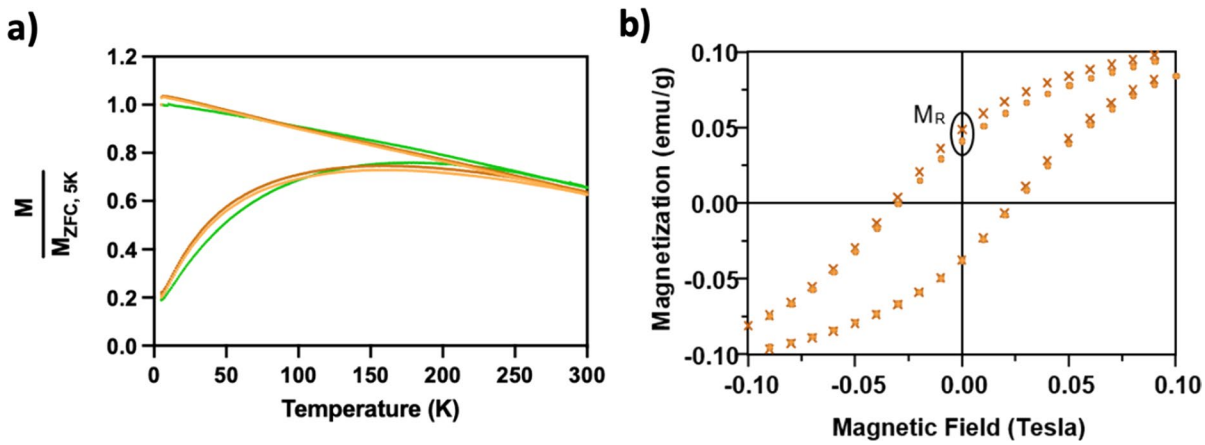

Fig. 7 Magnetic performance of aerogels: **a** ZFC–field cooled (FC) temperature dependent magnetization curves, and **b** magnetization *versus* field at 5 K of aerogels. BC-NF decorated with SPIONs (green) and incorporated into aerogels (orange and brown: two replicates of MC NF10-12 S aerogels)

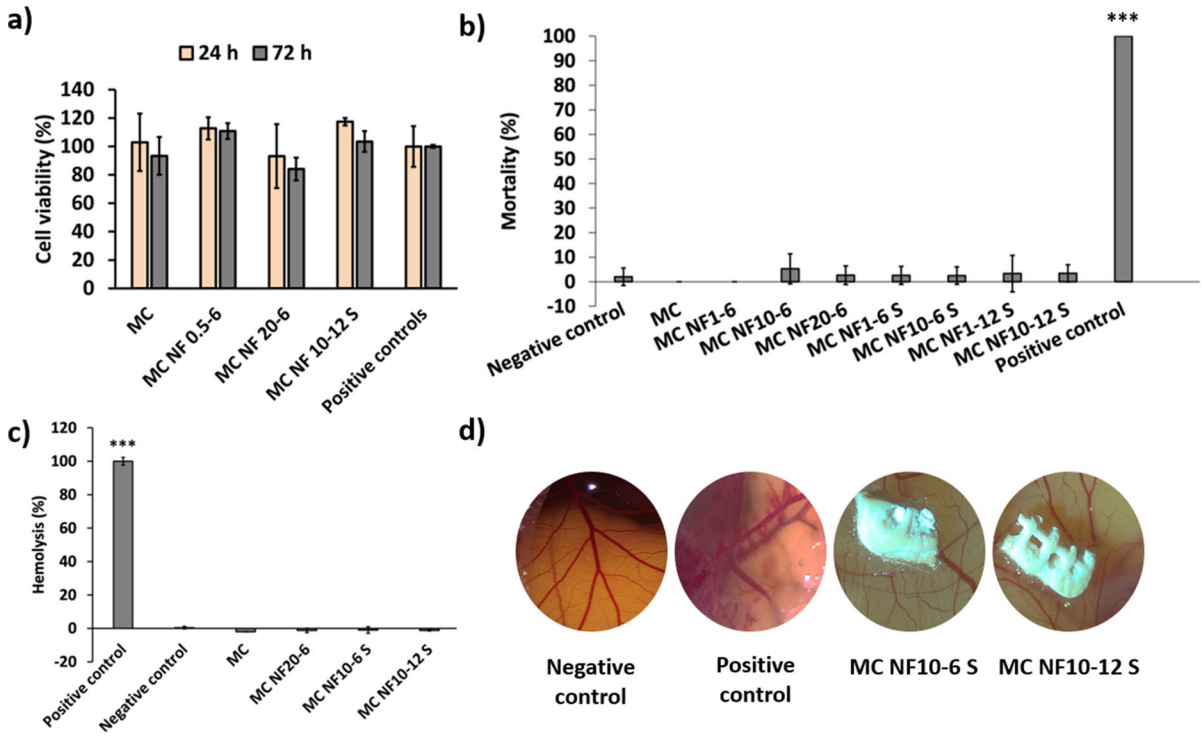

Fig. 8 Biological evaluation of cellulose-in-cellulose aerogels: **a** Viability of NIH/3T3 cells after 24 and 72 h of contact with aerogels, determined by Resazurin cytotoxicity assay. Positive control: NIH/3T3 cells **b** Mortality of *A. salina* after 24 h in contact with aerogels. Positive control: DMSO; negative control: artificial sea water. **c** Hemolytic activity tests of aerogels. Positive control: Triton; negative control: PBS pH 7.4. **d** HET-CAM test of aerogels. Negative control: PBS pH 7.4, positive control: 0.1N NaOH. Significant differences among groups were represented as * or ** (post hoc Tukey HSD multiple comparison test, $p < 0.05$ or $p < 0.01$, respectively)

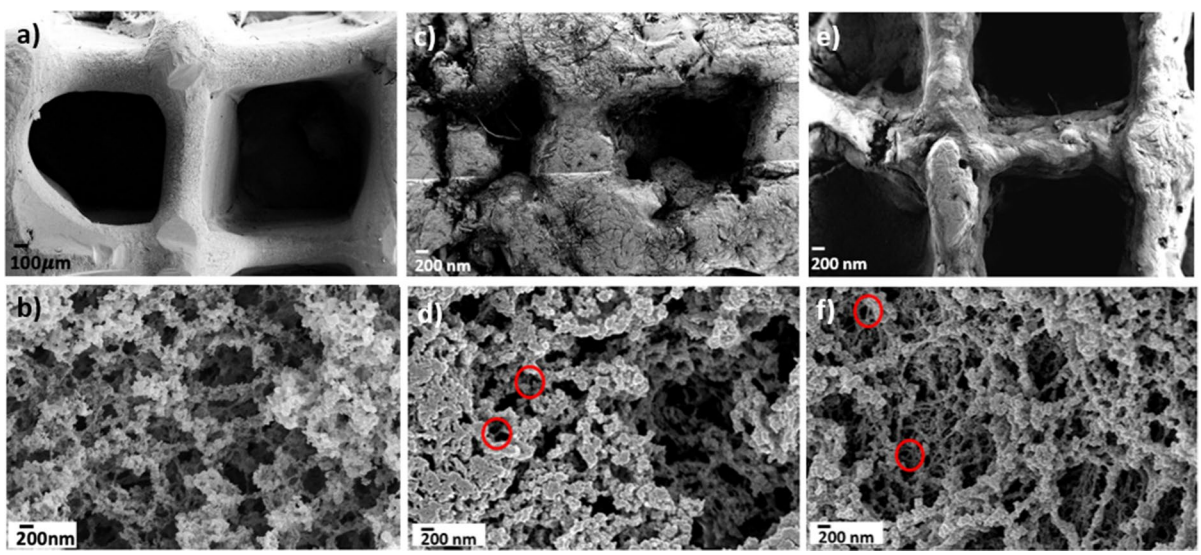

Fig. 9 SEM pictures of cellulose-in-cellulose aerogels after $scCO_2$ sterilization: **a, b** MC; **c, d** MC NF0.5–6 and **e, f** MC NF20-6. Aerogels imaged at two different magnifications. Red circles represent zones where the presence of BC-NF was detected by visual inspection

Conclusions

Dual porous cellulose-in-cellulose aerogels were obtained for the first time by combining 3D-printing and $scCO_2$ drying technologies. An enhancement in the printing fidelity (higher SFF) and an improvement in the structural resolution (lower volume shrinkage) were observed due to incorporating BC-NF into the aerogel structure. No detrimental effect on the viability of murine fibroblasts, hemolytic activity of human blood cells nor mortality of *A. salina* occurred after contact with cellulose-in-cellulose aerogels. Magnetic performance of SPIONs decorated aerogels was demonstrated and can be enhanced by doping with higher contents of these nanoparticles. Finally, either the $scCO_2$-based sterilization or storage for months of 3D-printed cellulose-in-cellulose aerogels did not have any detrimental effect on their physicochemical performance and validated this method for manufacturing sterilized cellulose-in-cellulose aerogel scaffolds. Magnetic properties achieved in this work opens up the avenue for unique structures, providing new understanding on the SPIONs' performance and its potential transitional application for bone tissue engineering. The reported results endorse the candidacy of these cellulose-based bioaerogels for bone tissue engineering applications.

Acknowledgments The authors want to express their gratitude to Thomas Meslier for preparing the SPIONs-loaded BC-NF.

Author contributions All authors contributed to the study conception and design. Material preparation, data collection and analysis were performed by Ana Iglesias-Mejuto, Nanthilde Malandain (BC-NF synthesis) and Tânia Ferreira-Gonçalves (preliminary safety tests). The first draft of the manuscript was written by Ana Iglesias-Mejuto and all authors commented on previous versions of the manuscript. All authors read and approved the final manuscript.

Funding This work was supported by Xunta de Galicia [ED431C 2020/17], MICINN [PID2020-120010RB-I00; PDC2022-133526-I00; PID2021-122645OB-I00], Agencia Estatal de Investigación [AEI], FEDER funds, 'Severo Ochoa' Programme for Center of Excellence in R&D (CEX2019-000917), and Generalitat de Catalunya (2021SGR00446 Grant). Work carried out in the framework of the COST Action IG18125 "Technical, commercial and societal innovations on aerogels towards circular economy" (ECO-AERoGELS) and funded by the European Commission. This work was also supported by Fundação para a Ciência e Tecnologia (FCT), Portugal, under the project references UIDB/00645/2020, UIDB/04138/2020 and UIDP/04138/2020. A.I.-M. acknowledges to Xunta de Galicia [ED481A-2020/104], N.M. to MICINN (PRE2019-089754, enrolled at the Biotechnology PhD program of the UABand), and T.F.-G. to Fundação para a Ciência e a Tecnologia, I.P. (FCT) [SFRH/BD/147306/2019] for their predoctoral research fellowships. N.M., A.L., and A.R. participate in the Spanish National Research Council (CSIC) interdisciplinary platform for sustainable plastics towards a circular economy (SusPlast), Nanomed Hub, Conexion Nanomedicina, Red Nanocare 2.0, and EPNOE network.

Availability of data and materials Data and materials are available upon request to the authors.

Declarations

Competing interests The authors have no relevant financial or non-financial interests to disclose.

Ethics approval Not applicable.

Consent to participate Not applicable.

Consent for publication All authors agree on the publication of this research work.

References

Ahlfeld T, Guduric V, Duin S et al (2020) Methylcellulose—a versatile printing material that enables biofabrication of tissue equivalents with high shape fidelity. Biomater Sci 8:2102–2110. https://doi.org/10.1039/D0BM00027B

Al-Jawuschi N, Chen S, Abie N et al (2023) Self-assembly-driven Bi 2 S 3 nanobelts integrated a silk-fibroin-based 3D-printed aerogel-based scaffold with a dual-network structure for photothermal bone cancer therapy. Langmuir 39:4326–4337. https://doi.org/10.1021/acs.langmuir.2c03334

Anastasova EI, Belyaeva AA, Tsymbal SA et al (2022) Hierarchical porous magnetite structures: from nanoparticle assembly to monolithic aerogels. J Colloid Interface Sci 615:206–214. https://doi.org/10.1016/j.jcis.2022.01.154

Arias SL, Shetty AR, Senpan A et al (2016) Fabrication of a functionalized magnetic bacterial nanocellulose with

iron oxide nanoparticles. J vis Exp 111:52951. https://doi.org/10.3791/52951
Athukoralalage SS, Balu R, Dutta NK, Roy Choudhury N (2019) 3D bioprinted nanocellulose-based hydrogels for tissue engineering applications: a brief review. Polymers 11:898. https://doi.org/10.3390/polym11050898
Bernardes BG, Del Gaudio P, Alves P et al (2021) Bioaerogels: promising nanostructured materials in fluid management. Healing and Regeneration of Wounds Molecules 26:3834. https://doi.org/10.3390/molecules26133834
Budtova T (2019) Cellulose II aerogels: a review. Cellulose 26:81–121. https://doi.org/10.1007/s10570-018-2189-1
Budtova T, Aguilera DA, Beluns S et al (2020) Biorefinery approach for aerogels. Polymers 12:2779. https://doi.org/10.3390/polym12122779
Charoensuk T, Sirisathitkul C, Boonyang U et al (2016) In vitro bioactivity and stem cells attachment of three-dimensionally ordered macroporous bioactive glass incorporating iron oxides. J Non Cryst Solids 452:62–73. https://doi.org/10.1016/j.jnoncrysol.2016.08.019
Chen Y, Zhang L, Yang Y et al (2021) Recent progress on nanocellulose aerogels: preparation, modification, composite fabrication. Applications Adv Mater 33:2005569. https://doi.org/10.1002/adma.202005569
Chiang W-H, Huang W-C, Chang C-W et al (2013) Functionalized polymersomes with outlayered polyelectrolyte gels for potential tumor-targeted delivery of multimodal therapies and MR imaging. J Control Release 168:280–288. https://doi.org/10.1016/j.jconrel.2013.03.029
Cochis A, Bonetti L, Sorrentino R et al (2018) 3D printing of thermo-responsive methylcellulose hydrogels for cell-sheet engineering. Materials 11:579. https://doi.org/10.3390/ma11040579
Corker A, Ng HC-H, Poole RJ, García-Tuñón E (2019) 3D printing with 2D colloids: designing rheology protocols to predict 'printability' of soft-materials. Soft Matter 15:1444–1456. https://doi.org/10.1039/C8SM01936C
Drobota M, Vlad S, Gradinaru LM et al (2022) Composite materials based on gelatin and iron oxide nanoparticles for MRI accuracy. Materials 15:3479. https://doi.org/10.3390/ma15103479
Feng Y, Zhu S, Mei D et al (2021) Application of 3D printing technology in bone tissue engineering: a review. Curr Drug Deliv 18:847–861. https://doi.org/10.2174/1567201817999201113100322
Ferreira-Gonçalves T, Iglesias-Mejuto A, Linhares T et al (2022) Biological thermal performance of organic and inorganic aerogels as patches for photothermal therapy. Gels 8:485. https://doi.org/10.3390/gels8080485
García-González CA, Fraile J, López-Periago A, Domingo C (2009) Preparation of silane-coated TiO2 nanoparticles in supercritical CO2. J Colloid Interface Sci 338:491–499. https://doi.org/10.1016/j.jcis.2009.06.035
García-González CA, Carenza E, Zeng M et al (2012) Design of biocompatible magnetic pectin aerogel monoliths and microspheres. RSC Adv 2:9816. https://doi.org/10.1039/c2ra21500d
Gerasimenko AYu, Zhurbina NN, Cherepanova NG et al (2020) Frame coating of single-walled carbon nanotubes in collagen on PET fibers for artificial joint ligaments. Int J Mol Sci 21:6163. https://doi.org/10.3390/ijms21176163
Gholami A, Ebrahiminezhad A, Abootalebi N, Ghasemi Y (2019) Synergistic evaluation of functionalized magnetic nanoparticles and antibiotics against staphylococcus aureus and *Escherichia coli*. Pharm Nanotechnol 6:276–286. https://doi.org/10.2174/2211738506666181031143048
Groult S, Buwalda S, Budtova T (2021) Pectin hydrogels, aerogels, cryogels and xerogels: influence of drying on structural and release properties. Eur Polym J 149:110386. https://doi.org/10.1016/j.eurpolymj.2021.110386
Hamidi MR, Jovanova B, Kadifkova Panovska T (2014) Toxicological evaluation of the plant products using Brine Shrimp (*Artemia salina* L.) model. Maced Pharm Bull 60:9–18. https://doi.org/10.33320/maced.pharm.bull.2014.60.01.002
Hu S, Zhou Y, Zhao Y et al (2018) Enhanced bone regeneration and visual monitoring via superparamagnetic iron oxide nanoparticle scaffold in rats. J Tissue Eng Regen Med 12:2085–2098. https://doi.org/10.1002/term.2641
Huang L, Du X, Fan S et al (2019) Bacterial cellulose nanofibers promote stress and fidelity of 3D-printed silk based hydrogel scaffold with hierarchical pores. Carbohydr Polym 221:146–156. https://doi.org/10.1016/j.carbpol.2019.05.080
Iglesias-Mejuto A, García-González CA (2021) 3D-printed alginate-hydroxyapatite aerogel scaffolds for bone tissue engineering. Mater Sci Eng C Mater Biol Appl 131:112525. https://doi.org/10.1016/j.msec.2021.112525
Iglesias-Mejuto A, García-González CA (2022) 3D-printed, dual crosslinked and sterile aerogel scaffolds for bone tissue engineering. Polymers 14:1211. https://doi.org/10.3390/polym14061211
Iglesias-Mejuto A, Magariños B, Ferreira-Gonçalves T, Starbird-Pérez R, Álvarez-Lorenzo C, Pinto Reis C, Ardao I, García-González CA (2024) Vancomycin-loaded methylcellulose aerogel scaffolds for advanced bone tissue engineering. Carbohydr Polym 324:121536. https://doi.org/10.1016/j.carbpol.2023.121536
Jin L, Zeng Z, Kuddannaya S et al (2016) Biocompatible, free-standing film composed of bacterial cellulose nanofibers-graphene composite. ACS Appl Mater Interfaces 8:1011–1018. https://doi.org/10.1021/acsami.5b11241
Karamat-Ullah N, Demidov Y, Schramm M et al (2021) 3D printing of antibacterial, biocompatible, and biomimetic hybrid aerogel-based scaffolds with hierarchical porosities via integrating antibacterial peptide-modified silk fibroin with silica nanostructure. ACS Biomater Sci Eng 7:4545–4556. https://doi.org/10.1021/acsbiomaterials.1c00483
Lagadec P, Balaguer T, Boukhechba F et al (2017) Calcium supplementation decreases BCP-induced inflammatory processes in blood cells through the NLRP3 inflammasome down-regulation. Acta Biomater 57:462–471. https://doi.org/10.1016/j.actbio.2017.05.039
Li H, Chen S (2015) Biomedical coatings on polyethylene terephthalate artificial ligaments. J Biomed Mater Res A 103:839–845. https://doi.org/10.1002/jbm.a.35218
Li Y, Xun X, Xu Y et al (2022) Hierarchical porous bacterial cellulose scaffolds with natural biomimetic nanofibrous

structure and a cartilage tissue-specific microenvironment for cartilage regeneration and repair. Carbohydr Polym 276:118790. https://doi.org/10.1016/j.carbpol.2021.118790

Linhares T, Pessoa De Amorim MT, Durães L (2019) Silica aerogel composites with embedded fibres: a review on their preparation, properties and applications. J Mater Chem A 7:22768–22802. https://doi.org/10.1039/C9TA04811A

López-Iglesias C, Barros J, Ardao I et al (2019) Vancomycin-loaded chitosan aerogel particles for chronic wound applications. Carbohydr Polym 204:223–231. https://doi.org/10.1016/j.carbpol.2018.10.012

Luo H, Li W, Ao H et al (2017) Preparation, structural characterization, and in vitro cell studies of three-dimensional SiO_2–CaO binary glass scaffolds built ofultra-small nanofibers. Mater Sci Eng C Mater Biol Appl 76:94–101. https://doi.org/10.1016/j.msec.2017.02.134

Luque-Michel E, Lemaire L, Blanco-Prieto MJ (2021) SPION and doxorubicin-loaded polymeric nanocarriers for glioblastoma theranostics. Drug Deliv and Transl Res 11:515–523. https://doi.org/10.1007/s13346-020-00880-8

Maleki H, Durães L, García-González CA et al (2016) Synthesis and biomedical applications of aerogels: possibilities and challenges. Adv Colloid Interface Sci 236:1–27. https://doi.org/10.1016/j.cis.2016.05.011

Manan S, Ullah MW, Ul-Islam M et al (2022) Bacterial cellulose: molecular regulation of biosynthesis, supramolecular assembly, and tailored structural and functional properties. Prog Mater Sci 129:100972. https://doi.org/10.1016/j.pmatsci.2022.100972

Mbituyimana B, Liu L, Ye W et al (2021) Bacterial cellulose-based composites for biomedical and cosmetic applications: Research progress and existing products. Carbohydr Polym 273:118565. https://doi.org/10.1016/j.carbpol.2021.118565

Mira-Cuenca C, Meslier T, Roig-Sanchez S et al (2021) Patterning bacterial cellulose films with iron oxide nanoparticles and magnetic resonance imaging monitoring. ACS Appl Polym Mater 3:4959–4965. https://doi.org/10.1021/acsapm.1c00723

Mortimer CJ, Wright CJ (2017) The fabrication of iron oxide nanoparticle-nanofiber composites by electrospinning and their applications in tissue engineering. Biotechnol J 12:1600693. https://doi.org/10.1002/biot.201600693

Nazari H, Heirani-Tabasi A, Hajiabbas M et al (2020) Incorporation of SPION-casein core-shells into silk-fibroin nanofibers for cardiac tissue engineering. J Cell Biochem 121:2981–2993. https://doi.org/10.1002/jcb.29553

Ng P, Pinho AR, Gomes MC et al (2022) Fabrication of antibacterial, osteo-inductor 3D printed aerogel-based scaffolds by incorporation of drug laden hollow mesoporous silica microparticles into the self-assembled silk fibroin biopolymer. Macromol Biosci 22:2100442. https://doi.org/10.1002/mabi.202100442

NIH Publication No. 10-7553 (2010) Recommended Test Method Protocol: Hen's Egg Test – Chorioallantoic Membrane (HET-CAM) Test Method

Oun AA, Shankar S, Rhim J-W (2020) Multifunctional nanocellulose/metal and metal oxide nanoparticle hybrid nanomaterials. Crit Rev Food Sci Nutr 60:435–460. https://doi.org/10.1080/10408398.2018.1536966

Panaitescu DM, Stoian S, Frone AN et al (2022) Nanofibrous scaffolds based on bacterial cellulose crosslinked with oxidized sucrose. Int J Biol Macromol 221:381–397. https://doi.org/10.1016/j.ijbiomac.2022.08.189

Pankhurst QA, Connolly J, Jones SK, Dobson J (2003) Applications of magnetic nanoparticles in biomedicine. J Phys D Appl Phys 36:167–181. https://doi.org/10.1088/0022-3727/36/13/201

Qu M, Wang C, Zhou X et al (2021) Multi-dimensional printing for bone tissue engineering. Adv Healthc Mater 10:2001986. https://doi.org/10.1002/adhm.202001986

Ribeiro N, Soares GC, Santos-Rosales V et al (2020) A new era for sterilization based on supercritical CO_2 technology. J Biomed Mater Res 108:399–428. https://doi.org/10.1002/jbm.b.34398

Roig-Sanchez S, Torrecilla O, Floriach-Clark J et al (2021) One-step biosynthesis of soft magnetic bacterial cellulose spheres with localized nanoparticle functionalization. ACS Appl Mater Interfaces 13:55569–55576. https://doi.org/10.1021/acsami.1c17752

Roig-Sanchez S, Kam D, Malandain N et al (2022) One-step double network hydrogels of photocurable monomers and bacterial cellulose fibers. Carbohydr Polym 294:119778. https://doi.org/10.1016/j.carbpol.2022.119778

Salerno A, Diéguez S, Diaz-Gomez L et al (2017) Synthetic scaffolds with full pore interconnectivity for bone regeneration prepared by supercritical foaming using advanced biofunctional plasticizers. Biofabrication 9:035002. https://doi.org/10.1088/1758-5090/aa78c5

Santos-Rosales V, Ardao I, Alvarez-Lorenzo C et al (2019) Sterile and dual-porous aerogels scaffolds obtained through a multistep supercritical CO_2-based approach. Molecules 24:871. https://doi.org/10.3390/molecules24050871

Santos-Rosales V, Magariños B, Starbird R et al (2021) Supercritical CO_2 technology for one-pot foaming and sterilization of polymeric scaffolds for bone regeneration. Int J Pharm 605:120801. https://doi.org/10.1016/j.ijpharm.2021.120801

Shin JY, Yeo YH, Jeong JE et al (2020) Dual-crosslinked methylcellulose hydrogels for 3D bioprinting applications. Carbohydr Polym 238:116192. https://doi.org/10.1016/j.carbpol.2020.116192

Shiu HT, Goss B, Lutton C et al (2014) Formation of blood clot on biomaterial implants influences bone healing. Tissue Eng Part B Rev 20:697–712. https://doi.org/10.1089/ten.teb.2013.0709

Shokouhimehr M, Theus AS, Kamalakar A et al (2021) 3D bioprinted bacteriostatic hyperelastic bone scaffold for damage-specific bone regeneration. Polymers 13:1099. https://doi.org/10.3390/polym13071099

Singh S, Singh G, Bala N, Aggarwal K (2020) Characterization and preparation of Fe3O4 nanoparticles loaded bioglass-chitosan nanocomposite coating on Mg alloy and in vitro bioactivity assessment. Int J Biol Macromol

151:519–528. https://doi.org/10.1016/j.ijbiomac.2020.02.208

Tang H, Kankala RK, Wang S, Chen A (2019) Supercritical fluid-assisted controllable fabrication of open and highly interconnected porous scaffolds for bone tissue engineering. Sci China Life Sci 62:1670–1682. https://doi.org/10.1007/s11427-018-9393-8

Theus AS, Ning L, Kabboul G et al (2022) 3D bioprinting of nanoparticle-laden hydrogel scaffolds with enhanced antibacterial and imaging properties. iScience 25:104947. https://doi.org/10.1016/j.isci.2022.104947

Wang X, Tang S, Chai S et al (2021) Preparing printable bacterial cellulose based gelatin gel to promote in vivo bone regeneration. Carbohydr Polym 270:118342. https://doi.org/10.1016/j.carbpol.2021.118342

Wang S, Zhao S, Yu J et al (2022) Advances in translational 3D printing for cartilage, bone, and osteochondral tissue engineering. Small 18:2201869. https://doi.org/10.1002/smll.202201869

Yang J, Zhou Y, Wei F, Xiao Y (2016) Blood clot formed on rough titanium surface induces early cell recruitment. Clin Oral Implants Res 27:1031–1038. https://doi.org/10.1111/clr.12672

Zeng M, Laromaine A, Roig A (2014) Bacterial cellulose films: influence of bacterial strain and drying route on film properties. Cellulose 21:4455–4469. https://doi.org/10.1007/s10570-014-0408-y

Zhang Y, Jiang S, Xu D et al (2023) Application of nanocellulose-based aerogels in bone tissue engineering: current trends and outlooks. Polymers 15:2323. https://doi.org/10.3390/polym15102323

Zhao N, Wang X, Qin L et al (2016) Effect of hyaluronic acid in bone formation and its applications in dentistry: effect of HA on cell proliferation and osteogenic differentiation. J Biomed Mater Res 104:1560–1569. https://doi.org/10.1002/jbm.a.35681